Three-Dimensional Single-Port Labyrinthine Acoustic Metamaterial: Perfect Absorption with Large Bandwidth and Tunability

Chi Zhang and Xinhua Hu*

Department of Materials Science, Key Laboratory of Micro- and Nano-Photonic Structures (Ministry of Education), and Laboratory of Advanced Materials, Fudan University, Shanghai 200433, China

(Received 22 July 2016; revised manuscript received 6 October 2016; published 29 December 2016)

Metamaterials are engineered materials which exhibit fascinating properties unreachable by traditional materials. Here, we report on the design, fabrication, and experimental characterization of a three-dimensional single-port labyrinthine acoustic metamaterial. By using curled perforations with one end closed and with appropriate loss inside, the metamaterial can perfectly absorb airborne sounds in a low-frequency band. Both the position and the relative width of the band can be tuned flexibly. A trade-off is uncovered between the relative absorption bandwidth and thickness of the metamaterial. When the relative absorption bandwidth is as high as 51%, the requirement of deep-subwavelength thickness (0.07λ) can still be satisfied. We emphasize that the perfect absorption with large tunability in relative bandwidth (from 9% to $> 180\%$) was not attainable previously and may find applications ranging from noise reduction to sound imaging.

DOI: 10.1103/PhysRevApplied.6.064025

I. INTRODUCTION

Acoustic metamaterials (AMMs) are artificial periodic structures with subwavelength building blocks that exhibit unusual acoustic characteristics [1–10]. There has been tremendous attention to AMMs since its first demonstration in 2000 by Liu *et al.* [1]. A number of functionalities and applications have been proposed and achieved based on AMMs [11–19]. Labyrinthine AMMs (LAMMs) composed of curled perforations are one of the most significant types of AMMs due to their extreme constitutive parameters and plentiful potential applications [20–25]. For instance, LAMMs show diverse properties such as double negativity, a density near zero, and a large refractive index in different frequencies, giving rise to fascinating phenomena, including negative refraction and zero-density tunneling [20–22]. By applying a graded structure, a labyrinthine metasurface with graded index can be constructed to modify the wave front and the direction of the outgoing waves [23,24]. Total reflection of low-frequency sounds was also achieved very recently by applying an ultrasparse labyrinthine metasurface [25]. To date, most of the studies have been done in two-dimensional (2D) cases, and the LAMMs usually have a two-port character so that transmission is permitted [20–25]. Although they are important in controlling sound waves in a three-dimensional (3D) space [26,27], 3D LAMMs have seldom been investigated and demonstrated.

In this paper, we report on the design, fabrication, and experimental characterization of 3D single-port LAMMs that are composed of curled, one-end-closed channels. Via adjusting the sound loss in channels to a critical value, such LAMMs can have impedance matching to the background and thus can perfectly absorb sounds in a low-frequency band; both the position and the relative width of the band can be tuned flexibly. Analytic formulas are derived to predict the critical loss in channels and the relative absorption bandwidth, and their accuracy is verified by both simulations and experiments. A trade-off is found between the relative absorption bandwidth and the thickness of the LAMM. When the relative absorption bandwidth is as high as 51%, the requirement of deep-subwavelength thickness (0.07λ) can still be satisfied (while the lateral sizes of a unit cell are 0.04λ).

Perfect absorption of waves is important to many applications, which has recently been a hot topic in the fields of wave physics and materials engineering [9,10,28]. Much effort has been devoted to construct perfect absorbers of electromagnetic and acoustic waves based on metamaterials with subwavelength thickness [9,10,28–32]. However, their relative absorption bandwidths are usually narrow and difficult to adjust. This work demonstrates perfect absorbers with large tunability in relative bandwidth (from 9% to $> 180\%$).

II. THEORY

To illustrate the principle, we first consider a 2D labyrinthine acoustic metasurface, which is a rigid slab with a channel array embedded [see Fig. 1(a)]. Unlike two-port labyrinthine AMMs [20–23,25], the labyrinthine metasurface here employs one-end-closed channels so that

*huxh@fudan.edu.cn

transmission is forbidden. The metasurface is perpendicular to the z direction, invariant along the y direction, and immersed in a background fluid where the sound velocity is c. The channels have a length of L, a width of w, and a period a along the x direction ($a \gg w$). Upon the metasurface is normally impinging a harmonic sound plane wave with wavelength $\lambda \gg a$ and frequency $f = c/\lambda$. Inside the channels, the wave number of sound $k_c = k(1 + i\beta)$, where $k = 2\pi/\lambda$ and β denotes the loss of sound (similar to the imaginary part of the refractive index in optics). When $w \ll \lambda$, the absorption does not change when the coiled channels become straight, as shown by the superposition of the solid and dotted lines in Fig. 1(e). For a system with straight channels, a coupled-mode theory can be applied (see Appendix A). If only fundamental modes are considered in both the channels and the background, the absorption of the metasurface can be analytically derived (see Appendix B),

$$A = 1 - |r|^2, \tag{1}$$

where the reflection coefficient $r = (1 - Z)/(1 + Z)$, the impedance of the metasurface relative to the background $Z = (w/a)[1 - \exp(i2k_cL)]/[1 + \exp(i2k_cL)]$, and i is the imaginary unity. Matched impedance ($Z = 1$) and thus unity absorption ($A = 1$) can be achieved when particular values of frequency and loss ($f = f_m$, $\beta = \beta_m$) are satisfied. Here, the resonant frequency f_m and critical loss β_m are given by (see Appendix B)

$$f_m = \frac{(2m-1)c}{4L}, \tag{2}$$

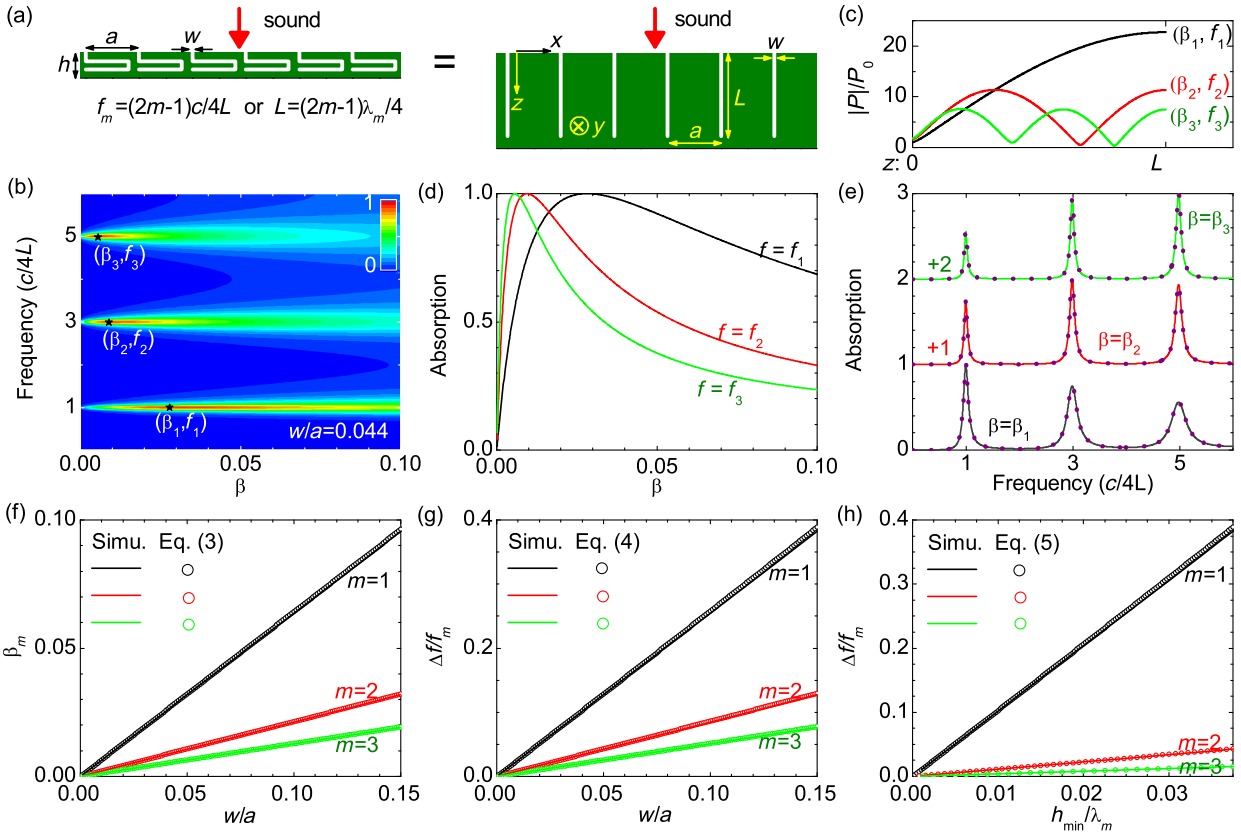

FIG. 1. The design principle of single-port LAMMs in 2D. (a) A rigid slab with a periodic array of curled, one-end-closed channels, which is embedded in a background fluid with a sound velocity of c (left panel). The channels have a width w, a length L, and a period a. The structure is invariant in the y direction. The slab is impinged normally by a plane sound wave with a wavelength λ, a frequency f, and a pressure P_0. The wave number is $k(1 + i\beta)$ in the channels, where $k = 2\pi/\lambda$ and β represents the loss. The acoustic absorption of the slab does not change when the channels become straight (right panel), as exemplified by (e). (b) Calculated absorption, shown in color, as a function of frequency f and loss β for the slab with $w/a = 0.044$ in (a). The absorption $A = 1$ when $f = f_m$ and $\beta = \beta_m$, with $m = 1, 2, 3$. (c) The distributions of acoustic pressure inside the channels for the situations with $A = 1$ in (b). (d),(e) Replotting of (b) along $f = f_m$ and $\beta = \beta_m$, respectively. The solid and dotted lines in (e) are results for straight and coiled channels, respectively. (f), (g) Optimal loss β_m and relative bandwidth $\Delta f/f_m$ as a function of channel width w, where Δf is the full width at half maximum of the mth absorption peak, with $\beta = \beta_m$. (h) Relative bandwidth $\Delta f/f_m$ as a function of $h_{\min}/\lambda_m$, where $\lambda_m = c/f_m$ and $h_{\min} = Lw/a$ is the minimal thickness of the slab with curled channels.

$$\beta_m = \frac{2w}{\pi(2m-1)a}, \tag{3}$$

where m is a positive integer ($m = 1, 2, 3\ldots$). Interestingly, the critical loss depends on the relative channel width w/a and does not rely on the channel length, while the critical decay length in channel is the same ($c/2\pi f_m\beta_m = La/w$) for any resonance order. The corresponding relative absorption bandwidth can also be analytically obtained:

$$\frac{\Delta f}{f_m} = \frac{8w}{\pi(2m-1)a}, \tag{4}$$

where Δf is the full width at half maximum for the mth-order absorption peak with $\beta = \beta_m$ (see Appendix B). When the rigid body has a minimal filling fraction in the metasurface, the metasurface has a minimal thickness $h_{\min} = Lw/a$, so that Eq. (4) can be rewritten as

$$\frac{\Delta f}{f_m} = \frac{32h_{\min}}{\pi(2m-1)^2\lambda_m}, \tag{5}$$

where $\lambda_m = c/f_m$ is the wavelength of the mth-order resonance. We note that, if the ratio of w/a is replaced by pq/a^2 [with p, q, and a defined in Figs. 2(a)–2(c)], the above formulas are also valid for a 3D labyrinthine metasurface. In particular, to achieve perfect absorption for the fundamental mode ($m = 1$) in 3D, the loss in channels should satisfy

$$\beta = \frac{2pq}{\pi a^2}. \tag{6}$$

We note that Eqs. (3)–(6) have not been derived previously and could be useful for dealing with similar systems [33].

III. SIMULATIONS

To verify the accuracy of the above formulas, we perform full-wave simulations for a 2D labyrinthine metasurface with parameters of $w = 0.044a$ and length $L = 6.7a$. The results are shown in Figs. 1(b)–1(e). We can see that the metasurface supports multiple resonant modes, with the frequencies agreeing well with Eq. (2). For the mth-order

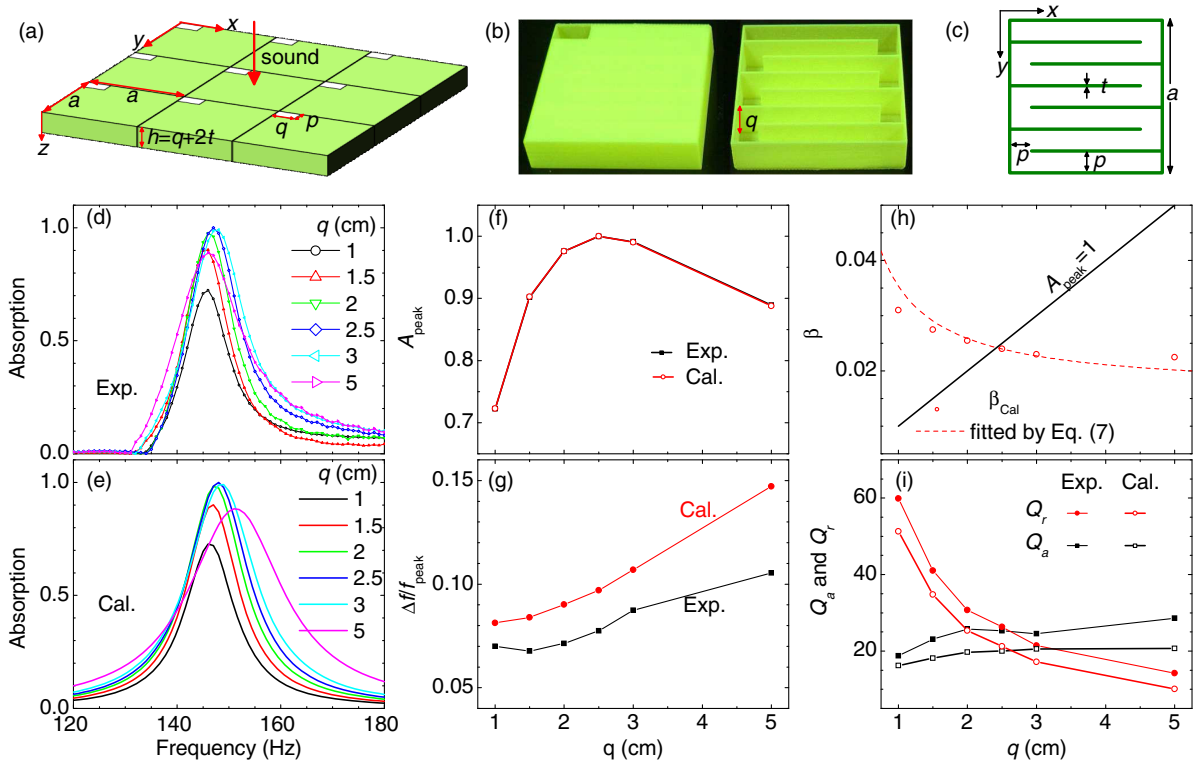

FIG. 2. Experimental realization of a 3D single-port LAMM with a narrow absorption band. (a) An acoustic metasurface that is immersed in air and impinged normally by a plane sound wave. The metasurface is periodic in the x-y plane and its unit cell has a size $a = 8.92$ cm in both the x and y directions and a height h in the z direction. A curled, one-end-closed channel exists in the unit cell and is connected to the outside via a rectangular aperture at the upper surface of the unit cell. The aperture has the same area as the cross section of the channel. (b) Photographs of a realistic unit cell fabricated with PLA by means of (left) 3D printing and (right) its inner structure. (c) Schematic illustration of the curled channel in the unit cell. The channel has a wall thickness $t = 1$ mm, a width $p = 1.16$ cm, and a height q. (d),(e) Measured and calculated absorption spectra for various heights of unit cells in (a). (f)–(i) Amplitude and relative width of the absorption peak (A_{peak} and $\Delta f/f_{\text{peak}}$), the loss β in the channel for achieving ideal and realistic absorption [the black line and the symbols in (h)], and the absorptive and radiative quality factors (Q_a and Q_r) of the unit cell as a function of the height h.

resonance [see Fig. 1(c)], there are m nodes (with local minimum) of sound pressure along the channel, which are also antinodes (with local maximum) of fluid velocity. Because of the friction between the fluid and channel walls, sound waves dissipate inside the channels. However, only when the sound loss inside the channel approaches critical values ($\beta = \beta_m$), the metasurface can totally absorb sound waves at resonant frequencies ($f = f_m$), as shown in Figs. 1(d) and 1(e).

Figures 1(f)–1(h) demonstrate the critical loss β_m inside channels and relative absorption bandwidths $\Delta f/f_m$ for different channel widths. Good agreement is found between the simulated and analytical results. Both the critical loss β_m and the relative absorption bandwidths $\Delta f/f_m$ are independent of the channel length and are related only to both the resonance order m and the relative channel width w/a. If a larger relative absorption bandwidth is desired, the fundamental mode ($m = 1$) is preferable while a larger relative channel width w/a and a higher critical loss β_1 should be applied.

IV. EXPERIMENTS

Experimentally, a high critical loss β_1 can be realized by placing some porous media (such as cotton) inside the channels. However, in the following, we consider a more interesting problem: whether perfect absorption with tunable bandwidth can be achieved in single-port LAMMs with hollow channels (i.e., without using porous media).

A. Single-channel case

Figure 2(a) shows a fabricated 3D labyrinthine metasurface which is periodic in the x-y plane and embedded in air. Its building block is a cuboid box fabricated with polylactic acid (PLA) by means of 3D-printing technology [see Fig. 2(b)]. The box has a fixed size of $a = 8.92$ cm in both the x and y directions and a height of h in the z direction. A curled channel is embedded inside the box [see Fig. 2(c)] and connected to outside via an aperture at the upper surface of the box. Both the opening and the cross section of the channel are rectangles with the same width of $p = 1.16$ cm and height of $q = h - 2t$, where the thickness $t = 1$ mm for all of the walls of the box and channels.

A series of building blocks have been fabricated with the channel height q ranging from 1 to 5 cm (see Appendix D), and their measured acoustic absorption spectra are shown in Fig. 2(d). We can see that absorption peaks occur at 146 Hz (thus, $a \approx 0.04\lambda$), corresponding to the $m = 1$ resonance of a channel with a length of $L = 58$ cm. Such an effective channel length is close to the realistic length of $7(a - 2t) = 61$ cm. The channel height has a small influence on the resonant frequency, while it strongly affects the amplitude of the absorption peak [see Fig. 2(f)]. When the channel height increases, the peak amplitude first increases, then decreases. When the channel height $q = 2.5$ cm (i.e., $q \approx 0.01\lambda$), the measured absorption can be as high as 99.9% at resonant frequency. In addition, the relative absorption peak width $\Delta f/f_{\text{peak}}$ increases with increasing channel height (or metasurface thickness). For a channel height q of 3 cm, the relative peak width can be 9%. We note that the performances of our structure, such as the measured peak absorption $A = 99.9\%$ and the ratio of metasurface thickness to wavelength $q \approx 0.01\lambda$, are superior to those of a similar structure whose measurements are $A = 90\%$ and $q \approx 0.02\lambda$ [33].

We applied a finite-element method to simulate the 3D labyrinthine metasurface (see Appendix C). The fundamental resonant frequency is first obtained by using a small sound loss in channels. Then the critical loss in channels is searched to achieve unity absorption at the resonant frequency, as shown by the solid line in Fig. 2(h). The simulated results are very close to the values in Eq. (6). The sound loss in channels is also obtained [see the symbols in Fig. 2(h)] by fitting the amplitudes of the calculated absorption peaks with the measured ones. We can see that the sound loss in channels decreases with an increase in the channel height q. The obtained sound loss from the measured absorption can be fitted by a simple model [34],

$$\beta = \beta_0 + 2g(p + q)/pq, \tag{7}$$

where $\beta_0 = 2 \times 10^{-5}$ is the sound loss due to the shear viscosity of air itself [34], and the second term with $g = 0.02$ cm is due to the friction (or shear viscosity) between the air molecules and the channel walls and is dominant here. Similar to the imaginary part of the refractive index of many optical materials (such as glass), β is also small and almost constant in a wide frequency range (e.g., from 100–1000 Hz), so that perfect absorption can be achieved at different peak frequencies [see Fig. 3(c)]. When the channel height $q = 2.5$ cm, the loss in channels approaches a critical value, leading to unity absorption at the resonant frequency [see Figs. 2(e) and 2(f)]. The relative peak width $\Delta f/f_{\text{peak}}$ is also found to increase with increasing channel height [see Fig. 2(g)].

Apart from the above first-principle microscopic simulation, the labyrinthine metasurface can also be understood by a macroscopic model, where the metasurface is regarded as a one-port resonator array with a reflection coefficient given by

$$r = 1 - \sum_m \frac{2Q_{r,m}^{-1}}{-i2(f/f_m - 1) + Q_{a,m}^{-1} + Q_{r,m}^{-1}}. \tag{8}$$

Here, $Q_{a,m} = \pi f_m t_{a,m}$ and $Q_{r,m} = \pi f_m t_{r,m}$ are the absorptive and radiative quality factors, respectively; $t_{a,m}$ and $t_{r,m}$ are the lifetimes of the resonance due to absorption inside the structure and radiation to the far field, respectively. For the $m = 1$ mode, the absorptive and radiative quality factors, Q_a and Q_r, are retrieved from the measured and

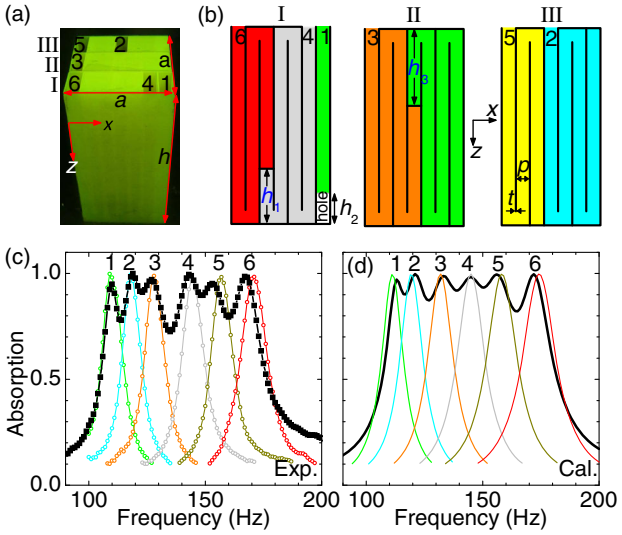

FIG. 3. Experimental realization of a 3D single-port LAMM with broadband absorption. (a) Photograph of the unit cell of acoustic metasurface. The unit cell has a size $a = 8.92$ cm in both the x and y directions and a height $h = 18$ cm, and it is composed of three parts that are fabricated with PLA by means of 3D printing. Six curled, one-end-closed channels exist in the unit cell and are connected to the outside via rectangular apertures of 2.84×1.16 cm at the upper surface of the unit cell. The lengths of the six channels are 49, 54, 59, 65, 72, and 79 cm, respectively. (b) Schematic illustration of the six channels (indicated with different colors) in the unit cell. The channels have a wall thickness $t = 1$ mm and width $p = 1.16$ cm. Other parameters are $h_1 = 5$ cm, $h_2 = 2.84$ cm, and $h_3 = 7$ cm. (c),(d) Measured and calculated absorption spectra of the unit cell (the thick curves). The results are also plotted when one aperture is open and others are closed in the unit cell (the thin curves).

simulated absorption (see Appendix C), as shown in Fig. 2(i). We can see that, with an increasing channel height q, the absorptive quality factor Q_a increases, while the radiative one Q_a decreases. When 2 cm $< q <$ 3.2 cm, the two quality factors are close to each other ($Q_a \approx Q_r$), so that the metasurface can absorb strongly ($A > 98\%$) incident sounds from the background medium of air at resonant frequency.

B. Multiple-channel case

The above experiments demonstrate that, when appropriate cross sections of channels are adopted, a labyrinthine metasurface with deep-subwavelength thickness ($h/\lambda = 1.2\%$) can totally absorb sounds at a resonant frequency of 146 Hz, holding a relative bandwidth of 9%. In the following, we show that the relative absorption bandwidth can be further broadened by applying various channels in the unit cell of the metasurface.

Figure 3(a) shows a fabricated cuboid unit cell with an unchanged size $a = 8.92$ cm in both the x and y directions and an increased height $h = 18.2$ cm in the z direction. Inside the unit cell, there exist six channels with the same cross section [$p = 2.84$ cm and $q = 1.16$ cm; see Fig. 3(b)]. The channel lengths are 78, 72, 66.4, 59.0, 54.1, and 49.7 cm, respectively.

Absorption spectra are first measured for unit cells with a single channel [see Fig. 3(c)], where one channel is hollow and the others are filled with water. We can see that the six channels individually contribute six absorption peaks, with central frequencies at 109, 118, 128, 144, 157, and 171 Hz, respectively. Similar to the channel lengths, the six resonant frequencies are also a geometric progression with a common ratio of 1.07. All six absorption peaks have amplitudes higher than 97% and an average width of about 9%. When all six channels are unblocked, the six peaks can merge together into an absorption band, with frequencies ranging from 105 to 177 Hz and a relative width of 51%. The thickness of the unit cell is much shorter than the central wavelength of the absorption band ($h/\lambda = 0.07$).

Although only six channels exist in the unit cell, as shown in Fig. 3(a), more channels can be adopted in the configuration. For an extreme situation with 21 channels, the first-order absorption band can possess a relative bandwidth as large as 180%. In addition, absorption bands with neighbored orders can overlap with each other, resulting in an ultrabroad absorption band ($A > 90\%$ for $f > f_c$) which is similar to that of a porous medium [35]. Hence, our 3D single-port LAMMs serve as a bridge linking damping resonant structures in a narrow band [9,10,33,36–38] and porous absorptive media for high frequencies [35]. We stress that the broadband perfect absorption observed here is not easy to achieve since, in many cases, resonators with small interspaces influence each other and the absorption can be suppressed by the spectral competition effects [39,40].

C. High absorption at oblique incidence

The observed strong absorption can also occur in a wide range of incident angles (see Fig. 4). Although the absorption decreases with an increasing incident angle θ, the peak absorption remains as high as 85% at $\theta = 75^0$ [see Fig. 4(a)]. The conclusion is also valid for the case of multiple channels with different lengths [see Fig. 4(b)].

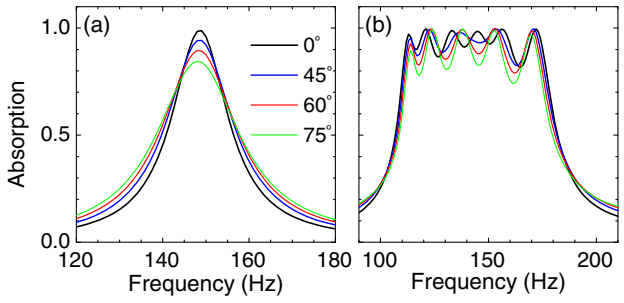

FIG. 4. Calculated absorption spectra at various incident angles. (a) and (b) represent the structures in Figs. 2 and 3, respectively.

V. SUMMARY

In this paper, we design, fabricate, and test a 3D single-port LAMM which can perfectly absorb airborne sound in a low-frequency band, when the sound loss in channels is adjusted to a critical value. In addition to its position, the relative width of the band can be changed in a very wide range (from 9% to > 180%). Such a new type of sound-absorbing materials serves as a bridge between traditional porous materials for high frequencies [35] and advanced damping resonant structures in a narrow band [9,10,33,36–38]. Our work presents a robust approach in controlling the sound loss in perforations and could benefit the experimental realizations of additional acoustic designs based on labyrinthine metamaterials.

ACKNOWLEDGMENTS

This work was supported by the 973 Program (Grants No. 2013CB632701 and No. 2012CB921604) and the NSFC (Grant No. 61422504).

APPENDIX A: COUPLED-MODE THEORY

Consider the 2D acoustic metasurface shown in the right panel of Fig. 1(a), which is invariant in the y direction and periodic along the x direction. The unit cell of the 2D metasurface is ranging from $0 < x < a$ (see Fig. 5). A rigid body exists in the green part, with $z < 0$ and $x < p$ or $x > p + w$. Fluid 1 exists in region I, with $z < 0$ and $0 < x < a$ (i.e., the background), while fluid 2 exists in region II with $z < 0$ and $p < x < p + w$ (i.e., the channel).

In region I, the acoustic pressure $P(z,x)$ satisfies $\nabla^2 P + k^2 P = 0$, so that we have $P = \sum_{j=-N}^{N} [C_j \exp(ik_{zj}z) + D_j \exp(-ik_{zj}z)] \exp(ik_{xj}x)$ for $z < 0$ and $0 < x < a$. Here, C_j and D_j represent the complex amplitude of incident and reflected waves, respectively, with $j = 0, \pm 1, \pm 2, \ldots, \pm N$. $k = \omega/c$, $c = \sqrt{B/\rho}$, B, and ρ are the wave number, sound velocity, bulk modulus, and mass density in region I, respectively. $k_z^2 + k_{xj}^2 = k^2$ and $k_{xj} = j2\pi/a$.

In region II, the acoustic pressure $P_c(z,x)$ satisfies $\nabla^2 P_c + k_c^2 P_c = 0$ with $\partial_x P_c = 0$ at $x = p$ and $p + w$. Hence, we have $P_c = \sum_{j=0}^{N_c} [E_j \exp(ik_{czj}z) + F_j \exp(-ik_{czj}z)] \cos[k_{cxj}(x-p)]$ for $z > 0$ and $p < x < p + w$. Here, E_j and F_j represent the complex amplitude of inward and outward waves, respectively, with $j = 0, 1, 2, \ldots, N_c$. $k_c = \omega/c_c$, $c_c = \sqrt{B_c/\rho_c}$, B_c, and ρ_c are the wave number, sound velocity, bulk modulus, and mass density in region II, respectively. $k_{czj}^2 + k_{cxj}^2 = k_c^2$ and $k_{cxj} = j\pi/a$.

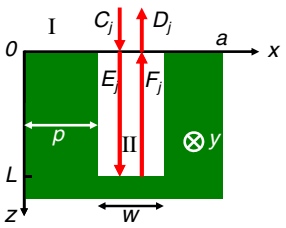

FIG. 5. The unit cell for the 2D acoustic metasurface shown in the right panel of Fig. 1(a).

The linking conditions at $z = 0$ are

$$P = P_c \quad \text{for } p < x < p + w, \tag{A1}$$

$$\rho^{-1}\frac{\partial}{\partial z}P = \left\{ \begin{array}{ll} 0 & \text{for } p > x \quad \text{or} \quad x > p + w \\ \rho_c^{-1}\frac{\partial}{\partial z}P_c & \text{for } p < x < p + w \end{array} \right\}. \tag{A2}$$

By substituting the expressions of P and P_c into Eqs. (A1) and (A2), multiplying Eq. (A1) with $\int_p^{p+w} \cos[k_{cxl_c}(x-p)]dx$ and Eq. (A2) with $\int_0^a \exp(-ik_{xl}x)dx$, then using $F_j = E_j \exp(i2k_{czj}L)$, we have

$$\sum_{N}^{j=-N} G_{1,l_cj}(C_j + D_j) = \sum_{j=0}^{N_c} G_{2,l_cj}[1 + \exp(i2k_{czj}L)]E_j, \tag{A3}$$

$$\sum_{j=-N}^{N} G_{3,lj}(C_j - D_j) = \sum_{j=0}^{N_c} G_{4,lj}[1 - \exp(i2k_{czj}L)]E_j. \tag{A4}$$

Here, $l_c = 0, 1, 2, \ldots, N_c$, $l = 0, \pm 1, \pm 2, \ldots, \pm N$, $G_{1,l_cj} = \int_p^{p+w} \cos[k_{cxl_c}(x-p)] \exp(ik_{xj}x)dx$, $G_{2,l_cj} = \int_p^{p+w} \cos[k_{cxl_c}(x-p)] \cos[k_{cxj}(x-p)]dx$, $G_{3,lj} = k_{zj}\rho^{-1} \int_0^a \exp(-ik_{xl}x) \exp(ik_{xj}x)dx$, and $G_{4,lj} = \rho_c^{-1}k_{czj} \int_p^{p+w} \exp(-ik_{xl}x) \cos[k_{cxj}(x-p)]dx$. By using $C_j = \delta_{j,0}$, D_j, E_j, reflection $R = |D_0/C_0|^2$, and absorption $A = 1 - R$ can be obtained.

APPENDIX B: DERIVATIONS OF EQS. (1)–(4)

When $N = N_c = 0$, Eqs. (A3) and (A4) become

$$G_1(C + D) = G_2[1 + \exp(i2k_cL)]E, \tag{B1}$$

$$G_3(C - D) = G_4[1 - \exp(i2k_cL)]E, \tag{B2}$$

where $G_1 = w$, $G_2 = w$, $G_3 = k\rho^{-1}a$, and $G_4 = k_c\rho_c^{-1}w$. Hence, we have

$$R \equiv \left|\frac{D}{C}\right|^2 = \left|\frac{1 - Z}{1 + Z}\right|^2, \tag{B3}$$

where $Z = (k_c\rho/k\rho_c)(w/a)[1 - \exp(i2k_cL)]/[1 + \exp(i2k_cL)]$. When $k_c\rho/k\rho_c \simeq 1$, we have $Z =$

$(w/a)[1-\exp(i2k_cL)]/[1+\exp(i2k_cL)]$. Thus, Eq. (1) can be obtained from $A=1-R$ and Eq. (B3).

The condition for $R=0$ (or $Z=1$) is

$$\exp(i2k_cL) = -(1-w/a)/(1+w/a). \quad \text{(B4)}$$

By using $k_c = k(1+i\beta)$, and thus $\exp(i2k_cL) = \exp(i2kL)\exp(-2k\beta L)$, the above equation becomes $\exp(i2kL) = -1$ [i.e., $2kL=(2m-1)\pi$, $m=1,2,3\ldots$] and $\exp(-2k\beta L)=(1-w/a)/(1+w/a)$ (i.e., $1-2k\beta L\simeq 1-2w/a$, when $w/a \ll 1$). Hence, we obtain Eqs. (2) and (3).

Assume $k=k_m+\Delta_k/2$, $k_m=(2m-1)\pi/2L$, and $\Delta_k/2 \ll k_m$. When Eq. (3) is satisfied, Eq. (B4) becomes $R=[2+2\cos(2kL)]/[v^2/u^2+u^2/v^2+2\cos(2kL)]$, where $u=1-w/a$ and $v=1+w/a$. Thus, the condition for $R=1/2$ is

$$\cos(2kL) = (v^2/u^2+u^2/v^2)/2-2. \quad \text{(B5)}$$

By using $(v^2/u^2+u^2/v^2)/2-2 \simeq -1+8(w/a)^2$ and $\cos(2kL)\simeq -1+\frac{1}{2}(\Delta_kL)^2$, Eq. (B5) becomes $\Delta_k = w/aL$, so that we have $\Delta_k/k_m = 8w/[\pi(2m-1)a]$, allowing Eq. (4) to be obtained.

APPENDIX C: DETAILS OF SIMULATIONS

With the exception of the dotted lines in Fig. 1(e), all of the results in Figs. 1(b)–1(h) are calculated by using the coupled-mode theory with $N=N_c/2=3$ in the right panel of Fig. 1(a). The results with $N=N_c/2=3$ are almost the same as those with $N=N_c=0$.

Other simulated results [the dotted lines in Figs. 1(e), 1(c), 2, and 3] are obtained by a finite-element method (COMSOL Multiphysics v4.3). Here, the mass density and the sound velocity of air are set as 1.29 kg/m^3 and 340 m/s, respectively; the mass density, Young's modulus and Poisson's ratio of PLA are set as 1.24×10^3 kg/m^3, 3.5 GPa, and 0.4, respectively. Since PLA and air are very different in density, simulated resonant frequencies change slightly ($<1\%$) when PLA is replaced by a rigid body. In experiments, the measured absorption spectra do not change when PLA is replaced by acrylonitrile butadiene styrene.

In the frequency ranges studied in Figs. 3(d) and 3(e), the fundamental ($m=1$) resonance dominates, so that Eqs. (7) and (8) can reduce as

$$A = \frac{4Q_a^{-1}Q_r^{-1}}{4(f/f_1-1)^2+(Q_a^{-1}+Q_r^{-1})^2}. \quad \text{(C1)}$$

By fitting the curves in Figs. 3(d) and 3(e) with this simplified equation, the resonant frequency f_1, the absorptive quality factor Q_a, and the radiative quality factor Q_r can be obtained for the $m=1$ resonance.

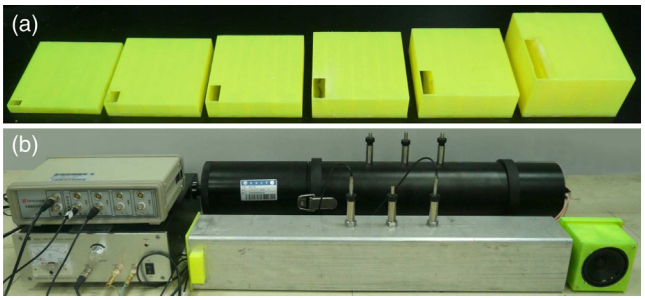

FIG. 6. (a) Photographs of six realistic unit cells fabricated with PLA by means of 3D printing. The unit cells are the same as those in Fig. 2(b), but with different q's ($q=1$, 1.5, 2, 2.5, 3, and 5 cm, from left to right). (b) Experimental setup of impedance tubes.

APPENDIX D: DETAILS OF EXPERIMENTS

The sample shown in the left panel of Fig. 2(b) is composed of a bottom part, as shown in the right panel of Fig. 2(b), and a square cover [see Fig. 6(a)]. The two parts are first fabricated with PLA by 3D-printing technology, then agglutinated together. Similarly, the sample shown in Fig. 3(a) is also fabricated.

A commercial impedance tube (Hangzhou Aihua, AWA6290T), which complies with ASTM C384-04 (2011) and ASTM E1050-12, was applied to measure the absorption of acoustic metasurfaces. Here, the impedance tube has a square cross section with a size of 9.05 cm, one (left) closed end and another (right) open end [see Fig. 6(b)]. Two 1/4-in. condensed microphones are situated at designated positions to sense local pressure. For each measurement, a unit cell of the metasurface is first placed at the left end of the tube, and a cubic box with a loudspeaker is then placed at the right end (so that the right end is also closed). The loudspeaker was fed with a sinusoidal signal of which the frequency increases with increasing time. By analyzing the signals from microphones, the absorption of the unit cell can be obtained by $A=1-|r|^2$, where r is the reflection coefficient of the unit cell.

[1] Z. Y. Liu, X. Zhang, Y. Mao, Y. Y. Zhu, Z. Yang, C. T. Chan, and P. Sheng, Locally resonant sonic materials, Science **289**, 1734 (2000).
[2] J. Li and C. T. Chan, Double-negative acoustic metamaterial, Phys. Rev. E **70**, 055602 (2004).
[3] Y. Lai, Y. Wu, P. Sheng, and Z. Q. Zhang, Hybrid elastic solids, Nat. Mater. **10**, 620 (2011).
[4] N. Fang, D. Xi, J. Xu, M. Ambati, W. Srituravanich, C. Sun, and X. Zhang, Ultrasonic metamaterials with negative modulus, Nat. Mater. **5**, 452 (2006).
[5] X. Hu, K. M. Ho, C. T. Chan, and J. Zi, Homogenization of acoustic metamaterials of Helmholtz resonators in fluid, Phys. Rev. B **77**, 172301 (2008).

[6] Z. Yang, J. Mei, M. Yang, N. H. Chan, and P. Sheng, Membrane-Type Acoustic Metamaterial with Negative Dynamic Mass, Phys. Rev. Lett. **101**, 204301 (2008).
[7] J. Mei, G. Ma, M. Yang, Z. Yang, W. Wen, and P. Sheng, Dark acoustic metamaterials as super absorbers for low-frequency sound, Nat. Commun. **3**, 756 (2012).
[8] M. Yang, G. Ma, Z. Yang, and P. Sheng, Coupled Membranes with Doubly Negative Mass Density and Bulk Modulus, Phys. Rev. Lett. **110**, 134301 (2013).
[9] G. Ma, M. Yang, S. Xiao, Z. Yang, and P. Sheng, Acoustic metasurface with hybrid resonances, Nat. Mater. **13**, 873 (2014).
[10] G. Ma and P. Sheng, Acoustic metamaterials: From local resonances to broad horizons, Sci. Adv. **2**, e1501595 (2016).
[11] J. Li, L. Fok, X. B. Yin, G. Bartal, and X. Zhang, Experimental demonstration of an acoustic magnifying hyperlens, Nat. Mater. **8**, 931 (2009).
[12] J. Zhu, J. Christensen, J. Jung, L. Martin-Moreno, X. Yin, L. Fok, X. Zhang, and F. J. Garcia-Vidal, A holey-structured metamaterial for acoustic deep-subwavelength imaging, Nat. Phys. **7**, 52 (2011).
[13] C. M. Park, J. J. Park, S. H. Lee, Y. M. Seo, C. K. Kim, and S. H. Lee, Amplification of Acoustic Evanescent Waves Using Metamaterial Slabs, Phys. Rev. Lett. **107**, 194301 (2011).
[14] M. H. Lu, X. K. Liu, L. Feng, J. Li, C. P. Huang, Y. F. Chen, Y. Y. Zhu, S. N. Zhu, and N. B. Ming, Extraordinary Acoustic Transmission through a 1D Grating with Very Narrow Apertures, Phys. Rev. Lett. **99**, 174301 (2007).
[15] J. Christensen, L. Martin-Moreno, and F. J. Garcia-Vidal, Theory of Resonant Acoustic Transmission through Subwavelength Apertures, Phys. Rev. Lett. **101**, 014301 (2008).
[16] R. Fleury and A. Alu, Extraordinary Sound Transmission through Density-Near-Zero Ultranarrow Channels, Phys. Rev. Lett. **111**, 055501 (2013).
[17] S. A. Cummer and D. Schurig, One path to acoustic cloaking, New J. Phys. **9**, 45 (2007).
[18] H. Chen and C. T. Chan, Acoustic cloaking in three dimensions using acoustic metamaterials, Appl. Phys. Lett. **91**, 183518 (2007).
[19] S. Zhang, C. Xia, and N. Fang, Broadband Acoustic Cloak for Ultrasound Waves, Phys. Rev. Lett. **106**, 024301 (2011).
[20] Z. Liang and J. Li, Extreme Acoustic Metamaterial by Coiling Up Space, Phys. Rev. Lett. **108**, 114301 (2012).
[21] Y. Xie, B. I. Popa, L. Zigoneanu, and S. A. Cummer, Measurement of a Broadband Negative Index with Space-Coiling Acoustic Metamaterials, Phys. Rev. Lett. **110**, 175501 (2013).
[22] Z. Liang, T. Feng, S. Lok, F. Liu, K. B. Ng, C. H. Chan, J. Wang, S. Han, S. Lee, and J. Li, Space-coiling metamaterials with double negativity and conical dispersion, Sci. Rep. **3**, 1614 (2013).
[23] Y. Xie, W. Wang, H. Chen, A. Konneker, B.-I. Popa, and S. A. Cummer, Wavefront modulation and subwavelength diffractive acoustics with an acoustic metasurface, Nat. Commun. **5**, 5553 (2014).
[24] K. Tang, C. Qiu, M. Ke, J. Lu, Y. Ye, and Z. Liu, Anomalous refraction of airborne sound through ultrathin metasurfaces, Sci. Rep. **4**, 6517 (2014).
[25] Y. Cheng, C. Zhou, B. G. Yuan, D. J. Wu, Q. Wei, and X. J. Liu, Ultra-sparse metasurface for high reflection of low-frequency sound based on artificial Mie resonances, Nat. Mater. **14**, 1013 (2015).
[26] T. Frenzel, J. D. Brehm, T. Buckmann, R. Schittny, M. Kadic, and M. Wegener, Three-dimensional labyrinthine acoustic metamaterials, Appl. Phys. Lett. **103**, 061907 (2013).
[27] Y. Li, G. Yu, B. Liang, X. Zou, G. Li, S. Cheng, and J. Cheng, Three-dimensional ultrathin planar lenses by acoustic metamaterials, Sci. Rep. **4**, 6830 (2014).
[28] C. M. Watts, X. Liu, and W. J. Padilla, Metamaterial electromagnetic wave absorbers, Adv. Mater. **24**, OP98 (2012).
[29] N. I. Landy, S. Sajuyigbe, J. J. Mock, D. R. Smith, and W. J. Padilla, Perfect Metamaterial Absorber, Phys. Rev. Lett. **100**, 207402 (2008).
[30] N. Liu, M. Mesch, T. Weiss, M. Hentschel, and H. Giessen, Infrared perfect absorber and its application as plasmonic sensor, Nano Lett. **10**, 2342 (2010).
[31] X. Xiong, S. C. Jiang, Y. H. Hu, R. W. Peng, and M. Wang, Structured metal film as a perfect absorber, Adv. Mater. **25**, 3994 (2013).
[32] G. M. Akselrod, J. Huang, T. B. Hoang, P. T. Bowen, L. Su, D. R. Smith, and M. H. Mikkelsen, Large-area metasurface perfect absorbers from visible to near-infrared, Adv. Mater. **27**, 8028 (2015).
[33] X. Cai, Q. Guo, G. Hu, and J. Yang, Ultrathin low-frequency sound absorbing panels based on coplanar spiral tubes or coplanar Helmholtz resonators, Appl. Phys. Lett. **105**, 121901 (2014).
[34] L. E. Kinsler, A. R. Frey, A. B. Coppens, and J. V. Sanders, *Fundamentals of Acoustics*, 4th ed. (John Wiley & Sons, New York, 2000).
[35] J. P. Arenas and M. J. Crocker, Recent trends in porous sound-absorbing materials, J. Sound Vib. **44**, 12 (2010).
[36] D.-Y. Maa, Potential of microperforated panel absorber, J. Acoust. Soc. Am. **104**, 2861 (1998).
[37] Y. Li and B. M. Assouar, Acoustic metasurface-based perfect absorber with deep subwavelength thickness, Appl. Phys. Lett. **108**, 063502 (2016).
[38] X. Wu, C. Fu, X. Li, Y. Meng, Y. Gao, J. Tian, L. Wang, Y. Huang, Z. Yang, and W. Wen, Low-frequency tunable acoustic absorber based on split tube resonators, Appl. Phys. Lett. **109**, 043501 (2016).
[39] S. Yi, M. Zhou, X. Shi, Q. Gan, J. Zi, and Z. Yu, A multiple-resonator approach for broadband light absorption in a single layer of nanostructured graphene, Opt. Express **23**, 10081 (2015).
[40] A. Merkel, G. Theocharis, O. Richoux, V. Romero-Garcia, and V. Pagneux, Control of acoustic absorption in one-dimensional scattering by resonant scatterers, Appl. Phys. Lett. **107**, 244102 (2015).